Available online at www.sciencedirect.com
ScienceDirect
Ocean Engineering 34 (2007) 1850–1862
OCEAN ENGINEERING
www.elsevier.com/locate/oceaneng

Propagation of monochromatic water wave trains

M. Hasanat Zaman[a,*], Hiroyoshi Togashi[b], R. Emile Baddour[a]

[a]National Research Council Canada, Institute for Ocean Technology, Arctic Ave., P.O. Box 12093, St. John's, NL, Canada A1B 3T5
[b]Department of Civil Engineering, Nagasaki University, 1-14 Bunkyo-Machi, Nagasaki City 852-8521, Japan

Received 7 June 2006; accepted 15 November 2006
Available online 14 February 2007

Abstract

A nonlinear numerical model has been formulated to study the propagation of a monochromatic surface wave. The model is formulated through the vertical integration of the continuity equation and the equations of motion. This model is investigated for wave propagation, velocity distribution, energy propagation and varying Courant, Friedrichs and Lewy's (CFL) condition. The applicability of this model for both shallow- and deep-water wave is also examined. The results and analyses are shown in details. The results obtained from the model are compared with the Stokes third-order wave theory and with the relevant experimental data.

Keywords: Vertically integrated model; Velocity distribution; Wave energy; Experiment

1. Introduction

Study of water wave propagation is always of interest to the coastal engineering practitioners and researchers. Traditionally the study of water waves may be classified into three major topics: (a) linear wave theory treats infinitesimal waves of arbitrary length. A detail description of the basic theory can be found in Lamb (1945) or Stoker (1957) or in other literatures. A sinusoidal wave in this category having considerably low slope can propagate long distances without changing its shape; (b) long wave theory assumes that the wavelength is larger than at least twice of the water depth. This category of wave may inherit considerable non-linearity and cannot propagate long distances without changing its shape. The characteristics of such waves are well described in many references. Ursell (1953), Peregrine (1967), Horikawa (1988), Cruz and Isobe (1994), Ohyama et al. (1995), Phillips (1997) are few to name and; (c) the last topic is a situation where the effects due to non-linearity and dispersion are significantly balanced and the wave can propagate quite long distances without major change in the wave forms.

These three categories of waves later become the basic tools used by scientists and researchers for the advancement of water waves theories from linear to nonlinear and, from very shallow- to very deep-water conditions. Again the wave propagation models can be of: (i) phase resolving models that are extensively adopted to study the non-linear shallow-water effects. For detail refer to Madsen and Sørensen (1993), Nwogu (1993) or others in relation to Boussinesq type models and for boundary value problem see Kaihatu and Kirby (1995) and Eldeberky and Madsen (1998), (ii) phase-averaged models are used in the open sea to study waves with essentially random phases, for example, see Battjes (1994), Herbers and Burton (1997) and Agnon and Sheremet (1997) and, (iii) typical vertically integrated type model see Beji and Nadaoka (2004), etc.

Researchers are finding more efficient tools to study different flow characteristics in the ocean. As stated in the above paragraph, a vast literature in this field is available, that contains various information about wave generation, propagation and decay for different given conditions. But still a lot more information is required to be known to update our present understanding in this field.

The present paper proposes to develop and illustrate an efficient numerical model that under some conditions can study wave fields both in shallow- and in deep-water regions. This model is formulated through the vertical

*Corresponding author.
E-mail address: Hasanat.Zaman@nrc-cnrc.gc.ca (M.H. Zaman).

0029-8018/$ - see front matter © 2007 Elsevier Ltd. All rights reserved.
doi:10.1016/j.oceaneng.2006.11.009

integration of the continuity equation and the equations of motion with the assumptions that the fluid is inviscid and incompressible. In the application of the obtained model both shallow- and deep-water conditions are considered separately. This model can be used more generally. It could be a useful tool in the study of the transformation of the ocean wave energy into electrical energy. In this study we have tested a range of waves from flat to steep to identify the limitations of this model.

2. Theory

2.1. Basic equations and coordinate system

For simplicity we consider a vertically two-dimensional wave field. The following continuity equation and equation of motions can describe the wave motion for an inviscid and incompressible fluid domain:

$$\frac{\partial u}{\partial x}+\frac{\partial w}{\partial z}=0, \tag{2.1}$$

$$\frac{\partial u}{\partial t}+\frac{\partial u^2}{\partial x}+\frac{\partial uw}{\partial z}+\frac{1}{\rho}\frac{\partial p}{\partial x}=0, \tag{2.2}$$

$$\frac{\partial w}{\partial t}+\frac{\partial uw}{\partial x}+\frac{\partial w^2}{\partial z}+\frac{1}{\rho}\frac{\partial p}{\partial z}+g=0, \tag{2.3}$$

where u and w are velocity components in the x and z direction, g the acceleration due to gravity and ρ is the water density. The total pressure p is the summation of p_s, the hydrostatic pressure below the mean water level (MWL) and p_d the dynamic pressure due to wave motion on the free surface.

Fig. 1 shows the coordinate system. d is the instantaneous water depth, h the still water depth ($z=0$); δ represents the deviation of the MWL from the still water level (SWL) if any due to, for instance, wave motion over any uneven sea bottom.

2.2. Velocity potential, boundary conditions and pressure

2.2.1. Velocity potential

A velocity potential Φ_w is adopted on the assumption that this form is capable to express the characteristics of a wave field upon satisfying suitable boundary conditions. See Dean and Dalrymple (1992) for example. It is written in the form

$$\Phi_w = A\cosh k(h+z)\cos(kx-\sigma t), \tag{2.4}$$

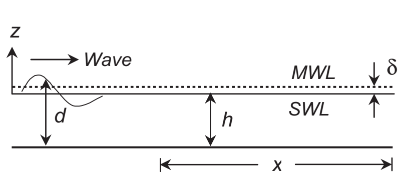

Fig. 1. Coordinate system.

where A is a constant related to wave amplitude, h the still water depth, k the wave number, σ the angular frequency, z the vertical axis and t is the elapsed time.

2.2.2. Dynamic boundary condition and pressure

The surface elevation η can be obtained from the following surface boundary condition:

$$\eta = -\frac{1}{g}\left[\frac{\partial \Phi_w}{\partial t}+\frac{1}{2}\left(\frac{\partial \Phi_w}{\partial x}\right)^2+\frac{1}{2}\left(\frac{\partial \Phi_w}{\partial z}\right)^2\right]. \tag{2.5}$$

Substituting Eq. (2.4) into Eq. (2.5) one can find the surface elevation as follows:

$$\eta = -\frac{A\sigma}{g}\cosh k(h+z)\sin(kx-\sigma t)-\frac{1}{2g}A^2k^2[\sin^2(kx-\sigma t)] \\ -\frac{1}{2g}A^2k^2[\sinh^2 k(h+z)], \tag{2.6}$$

$$\Rightarrow \eta = -\frac{A\sigma}{g}\cosh k(h+\eta)\sin(kx-\sigma t) \\ -\frac{1}{2g}A^2k^2[\sin^2(kx-\sigma t)]_{z=\eta} \\ -\frac{1}{2g}A^2k^2[\sinh^2 k(h+\eta)]_{z=\eta}. \tag{2.7}$$

The dynamic pressure equation can be formulated from Bernoulli equation in the following manner:

$$p_d = -\rho\left[\frac{\partial \Phi_w}{\partial t}+\frac{1}{2}\left(\frac{\partial \Phi_w}{\partial x}\right)^2+\frac{1}{2}\left(\frac{\partial \Phi_w}{\partial z}\right)^2\right], \tag{2.8}$$

$$\Rightarrow \frac{p_d}{\rho} = -A\sigma\cosh k(h+z)\sin(kx-\sigma t) \\ -\frac{1}{2}A^2k^2[\sin^2(kx-\sigma t)] \\ -\frac{1}{2}A^2k^2[\sinh^2 k(h+z)]. \tag{2.9}$$

In Eq. (2.7) the wave induced component, A^2k^2 would be negligibly small for waves with relatively small amplitudes and/or large wavelengths. When all the terms associated with A^2k^2 are neglected then Eq. (2.7) can be simplified as follows:

$$\eta = -\frac{A\sigma}{g}\cosh k(h+\eta)\sin(kx-\sigma t). \tag{2.10}$$

In a similar fashion when A^2k^2 are neglected and Eq. (2.10) is invoked then Eq. (2.9) takes the following form (Dean and Dalrymple, 1992):

$$\frac{p_d}{\rho} = g\eta\frac{\cosh k(h+z)}{\cosh kd}, \tag{2.11}$$

where g is the gravitational acceleration and $d=h+\eta$ is the instantaneous water depth shown in Fig. 1.

2.2.3. Dispersion relation

The angular frequency σ and the wave number k are interdependent through the dispersion relation. The dispersion relation can be obtained from the following kinematic condition when the expressions for Φ_w and η are substituted:

$$\frac{\partial \Phi_w}{\partial z} = \frac{\partial \eta}{\partial t} + \frac{\partial \Phi_w}{\partial x}\frac{\partial \eta}{\partial x}. \tag{2.12}$$

Again neglecting the term associated with A^2k^2 the following dispersion relation can be obtained:

$$\sigma^2 = gk \tanh kd. \tag{2.13}$$

The unknown wave number k would be computed from this relation when the wave period T $(= 2\pi/\sigma)$ and the local water depth d are known.

2.2.4. Kinematic boundary condition

The kinematic boundary conditions that must be satisfied on the free surface and at the bottom are

$$\frac{\partial \eta}{\partial t} + u_\eta \frac{\partial \eta}{\partial x} = w_\eta \quad \text{at } z = \eta, \tag{2.14}$$

$$u_{-h}\frac{\partial h}{\partial x} = -w_{-h} \quad \text{at } z = -h, \tag{2.15}$$

where the subscripts η and $-h$ express the respective quantity at the free surface and at the bottom.

2.3. Vertical integration of the basic equations

The governing equations of the present model are obtained after the vertical integration of Eqs. (2.1) and (2.2) in the following steps:

$$\int_{-h}^{\eta} \frac{\partial u}{\partial x}\,\mathrm{d}z + \int_{-h}^{\eta} \frac{\partial w}{\partial z}\,\mathrm{d}z = 0. \tag{2.16}$$

Applying Leibnize's integration method and invoking the kinematic free surface and bottom boundary conditions (Eqs. (2.14) and (2.15)) the continuity equation, Eq. (2.1) takes the following form:

$$\Rightarrow \frac{\partial}{\partial x}\int_{-h}^{\eta} u\,\mathrm{d}z - \frac{\partial \eta}{\partial x}u_\eta - \frac{\partial h}{\partial x}u_{-h} + w_\eta - w_{-h} = 0, \tag{2.17}$$

$$\Rightarrow \frac{\partial}{\partial x}\int_{-h}^{\eta} u\,\mathrm{d}z + \frac{\partial \eta}{\partial t} = 0, \tag{2.18}$$

$$\Rightarrow \frac{\partial \eta}{\partial t} + \frac{\partial P}{\partial x} = 0, \tag{2.19}$$

where $P = \int_{-h}^{\eta} u\,\mathrm{d}z$ is the discharge per unit water depth.

In a similar fashion the momentum equation in the x-direction may be obtained in the following way from Eq. (2.2):

$$\int_{-h}^{\eta} \frac{\partial u}{\partial t}\,\mathrm{d}z + \int_{-h}^{\eta} \frac{\partial u^2}{\partial x}\,\mathrm{d}z + \int_{-h}^{\eta} \frac{\partial uw}{\partial z}\,\mathrm{d}z + \int_{-h}^{\eta} \frac{1}{\rho}\frac{\partial p}{\partial x}\,\mathrm{d}z = 0, \tag{2.20}$$

$$\begin{aligned}\Rightarrow & \frac{\partial}{\partial t}\int_{-h}^{\eta} u\,\mathrm{d}z - \frac{\partial \eta}{\partial t}u_\eta - \frac{\partial h}{\partial t}u_{-h} + \frac{\partial}{\partial x}\int_{-h}^{\eta} u^2\,\mathrm{d}z \\ & - \frac{\partial \eta}{\partial x}u_\eta^2 - \frac{\partial h}{\partial x}u_{-h}^2 + u_\eta w_\eta - u_{-h}w_{-h} \\ & + \frac{\partial}{\partial x}\int_{-h}^{\eta} \frac{p}{\rho}\,\mathrm{d}z - \frac{\partial \eta}{\partial x}\left(\frac{p}{\rho}\right)_\eta - \frac{\partial h}{\partial x}\left(\frac{p}{\rho}\right)_{-h} = 0,\end{aligned} \tag{2.21}$$

$$\begin{aligned}\Rightarrow & \frac{\partial}{\partial t}\int_{-h}^{\eta} u\,\mathrm{d}z + \frac{\partial}{\partial x}\int_{-h}^{\eta} u^2\,\mathrm{d}z + \frac{\partial}{\partial x}\int_{-h}^{\eta} \frac{p}{\rho}\,\mathrm{d}z \\ & - \frac{\partial \eta}{\partial x}\left(\frac{p}{\rho}\right)_\eta - \frac{\partial h}{\partial x}\left(\frac{p}{\rho}\right)_{-h} = 0.\end{aligned} \tag{2.22}$$

For convenience the following momentum correction factor *see* for example Hager (1983), Yu (1990) and Beecham et al. (2005) is introduced into the above momentum equation:

$$\gamma = \frac{\mathrm{d}}{\int_{-h}^{\eta} u\,\mathrm{d}z \int_{-h}^{\eta} u\,\mathrm{d}z}\int_{-h}^{\eta} u^2\,\mathrm{d}z. \tag{2.23}$$

The magnitude of γ depends on the vertical distribution of the horizontal velocity component u, which may be expressed by the following relationship:

$$u = u_{z=-h}\cosh k(h+z). \tag{2.24}$$

Substituting Eq. (2.24) in Eq. (2.23) and after the integration we can obtain the momentum correction factor as follows:

$$\gamma = \frac{kd}{2\tanh kd}\left[1 + \frac{2kd}{\sinh 2kd}\right]. \tag{2.25}$$

The dynamic pressure related parameters are summarized in the following forms from Eq. (2.11) along with Eq. (2.30):

$$\frac{1}{g}\int_{-h}^{\eta} \frac{p_d}{\rho}\,\mathrm{d}z = \int_{-h}^{\eta} \eta\frac{\cosh k(h+z)}{\cosh kd}\,\mathrm{d}z = \frac{\eta}{k}\tanh kd = \frac{\eta}{g}C_w^2, \tag{2.26}$$

$$\frac{1}{g}\left(\frac{p_d}{\rho}\right)_\eta = \left(\eta\frac{\cosh k(h+z)}{\cosh kd}\right)_{z=\eta} = \eta, \tag{2.27}$$

$$\frac{1}{g}\left(\frac{p_d}{\rho}\right)_{-h} = \left(\eta\frac{\cosh k(h+z)}{\cosh kd}\right)_{z=-h} = \frac{\eta}{\cosh kd}. \tag{2.28}$$

Substituting Eqs. (2.25)–(2.28) into Eq. (2.22) we can find the momentum equation in the following shape:

$$\frac{\partial P}{\partial t} + \frac{\partial}{\partial x}\left(\gamma\frac{P^2}{d}\right) + (\eta g\beta_1 + C_w^2)\frac{\partial \eta}{\partial x} + \eta g\beta_2\frac{\partial h}{\partial x} = 0, \tag{2.29}$$

where C_w is the local wave celerity and, β_1 and β_2 are the relative water depth dependent parameters:

$$C_w = \sigma/k = \sqrt{\frac{g}{k}\tanh kd}, \tag{2.30}$$

$$\beta_1 = F\left[\frac{\mathrm{e}^{4kd} + 2\mathrm{e}^{2kd}\sinh 2kd - 1}{\mathrm{e}^{4kd} + 4\mathrm{e}^{2kd}kd - 1}\right] - 1, \tag{2.31}$$

$$\beta_2 = F\left[\frac{e^{4kd} + 2e^{2kd}\sinh 2kd - 1}{e^{4kd} + 4e^{2kd}kd - 1}\right] - \frac{1}{\cosh kd}, \tag{2.32}$$

$F = 1 - \tanh^2 kd.$

Finally Eqs. (2.19) and (2.29) are obtained as our governing equations for the proposed research.

2.4. Derivation of pressure from z-direction momentum equation

Eq. (2.11) can also be obtained from Eq. (2.3). The momentum equation in the z-direction (Eq. (2.3)) establishes a relation between the fluid pressure and the water surface elevation. Assuming that the vertical acceleration and advective terms in the above equation are negligible in comparison with the other terms, then Eq. (2.3) takes the following form:

$$\frac{1}{\rho}\frac{\partial p}{\partial z} + g = 0, \tag{2.33}$$

$$\Rightarrow \frac{1}{\rho}\frac{\partial p}{\partial z} = -g, \tag{2.34}$$

$$\Rightarrow p = -\rho g z + C'(x,t), \tag{2.35}$$

$$\Rightarrow C'(x,t) = \rho g \eta|_{at\ z=\eta, p=0}, \tag{2.36}$$

$$\Rightarrow \frac{p}{\rho} = -gz + g\eta, \tag{2.37}$$

$$\Rightarrow \left(\frac{p}{\rho}\right)_z = -gz + g\eta\frac{\cosh k(h+z)}{\cosh kd}, \tag{2.38}$$

where $C'(x,t)$ is an integration constant. The term $\cosh k(h+z)/\cosh kd$ introduced in the dynamic pressure equation is called a pressure response factor (Sarpkaya and Issscson, 1981; Dean and Dalrymple, 1992). The above term is required to evaluate the vertical distribution of the dynamic pressure. This term has unit value at the surface ($z = \eta$) but varies along the water depth.

$$\Rightarrow \left(\frac{p_s}{\rho}\right)_z + \left(\frac{p_d}{\rho}\right)_z = -gz + g\eta\frac{\cosh k(h+z)}{\cosh kd}, \tag{2.39}$$

$$\Rightarrow \left(\frac{p_s}{\rho}\right)_z = -gz, \tag{2.40}$$

$$\Rightarrow \left(\frac{p_d}{\rho}\right)_z = g\eta\frac{\cosh k(h+z)}{\cosh kd}. \tag{2.41}$$

Splitting Eq. (2.39) gives two pressure components of the system of which Eq. (2.40) represents the static pressure component and Eq. (2.41) stands for the dynamic pressure. It may be observed that Eq. (2.41) is identical to Eq. (2.11). It may be noted from Eq. (2.11) or (2.41) that the hyperbolic cosine terms in the denominators adapted the instantaneous water depth instead of the still water depth. This kind of modification was introduced by Hedges (1976) to improve the propagation speed of wave having relatively large wave amplitude by the small amplitude wave theory. The above pressure equation has insignificant influence on the deep-water wave but it significantly improves the pressure distribution for shallow-water region.

To generalize the formulation we introduce a variable δ in the pressure equations to represent the deviation of the MWL from the SWL if any due to, for instance, wave motion over any uneven sea bottom. Eqs. (2.40) and (2.41) could then be rewritten in the following forms:

$$p_s = \rho g(\delta - z), \tag{2.42}$$

$$p_d = \rho g(\eta - \delta)\frac{\cosh k(h+z)}{\cosh kd}. \tag{2.43}$$

The periodic free surface elevation η can be expressed to first order in amplitude a as

$$\eta = a\sin(kx - \sigma t). \tag{2.44}$$

2.5. Numerical scheme

Discretization of Eqs. (2.19) and (2.29) are performed following a semi-implicit finite difference technique described by Dronkers (1969). The computational mesh in the x–t plane is shown in Fig. 2. The discharge P is defined at the integer grid points and fractional time steps (shown by solid circles in the mesh) and those of η are defined at the fractional grid points and integer time steps (shown by solid squares in the mesh). After discretization Eqs. (2.19) and (2.29) take the following forms (for details *see* Zaman and Togashi, 1997):

$$\frac{\eta^{n+1}_{j+1/2} - \eta^{n}_{j+1/2}}{\Delta t} + \frac{P^{n+1/2}_{j+1} - P^{n+1/2}_{j}}{\Delta x} = 0, \tag{2.45}$$

$$A^{n+1}_j P^{n+3/2}_{j-1} + B^{n+1}_j P^{n+3/2}_j + C^{n+1}_j P^{n+3/2}_{j+1} - D^{n+1}_j = 0, \tag{2.46}$$

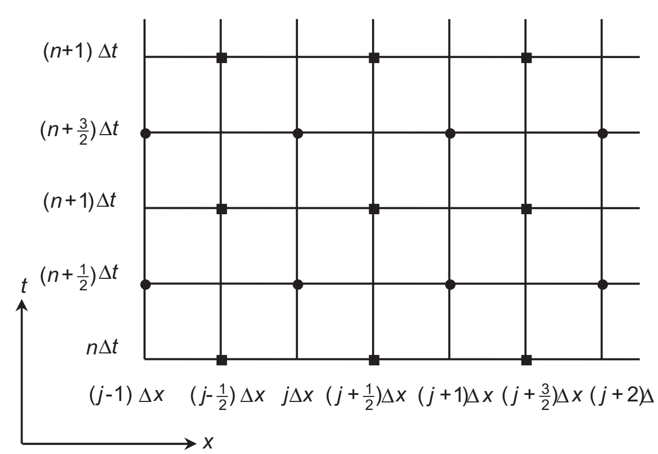

Fig. 2. Computational mesh.

where A, B, C and D are numerical constants; Δt and Δx are the temporal and spatial increments, respectively; n and j are the time and spatial steps, respectively, and can be obtained as

$$A_j^{n+1} = -\frac{\Delta t}{4\Delta x}\left[\frac{\gamma}{d}\right]_{j-1/2}^{n+1}[P_j + P_{j-1}]^{n+1/2}, \tag{2.47}$$

$$C_j^{n+1} = \frac{\Delta t}{4\Delta x}\left[\frac{\gamma}{d}\right]_{j-1/2}^{n+1}[P_{j+1} + P_j]^{n+1/2}, \tag{2.48}$$

$$B_j^{n+1} = 1 + A_j^{n+1} + C_j^{n+1}, \tag{2.49}$$

$$\begin{aligned} D_j^{n+1} = P_j^{n+1/2} &- \frac{\Delta t}{2\Delta x}[(C_w^2 + \beta_1 g\eta)_{j+1/2}^{n+1} \\ &+ (C_w^2 + \beta_1 g\eta)_{j-1/2}^{n+1}][\eta_{j+1/2}^{n+1} - \eta_{j-1/2}^{n+1}] \\ &- \frac{g\Delta t}{2\Delta x}[(\beta_2\eta)_{j+1/2}^{n+1} + (\beta_2\eta)_{j-1/2}^{n+1}] \\ &\times [h_{j+1/2} - h_{j-1/2}]^{n+1}. \end{aligned} \tag{2.50}$$

The model obtained here is very direct as the discretized continuity equation is of explicit nature. The momentum equation constructs a tridiagonal coefficient matrix at every time step that can be efficiently solved by double sweep algorithm. In the application of this model the number of grid points must be odd for the consistency with the numerical scheme.

2.6. Boundary conditions and procedure of computation

As the initial condition ηs at $n\Delta t$ time level and Ps at $(n+\frac{1}{2})\Delta t$ time level are known on the relevant grid points in the whole computational domain. Boundary condition is employed in terms of discharge P on the incident boundary at the first grid point and on the transmitted boundary at the last grid point. As the time progresses the system takes control and computes ηs and Ps at all designated grid points until it reaches at the given end-time limit. The computational tactics of this model is, ηs at time level $(n+1)\Delta t$ will be evaluated by Eq. (2.45) with the known values of ηs at time level $n\Delta t$ and, Ps at $(n+\frac{1}{2})\Delta t$ time level and then, Eq. (2.46) is employed to estimate Ps for $(n+\frac{3}{2})\Delta t$ time level, using the calculated ηs at $(n+1)\Delta t$ time level. The coupling of the above equations will continue until a steady state is reached.

2.7. Stability of the scheme

The stability of any numerical model is very important issue for its reliability and/or range of application. It is very difficult to ensure that a particular model is unconditionally stable. It may be stable for the conditions considered but may not be stable for some other unknown conditions. To predict the stability of the present model, a standard method is adopted to observe the growth and propagation of any infinitesimal disturbance introduced to the solution at any time of the computation. Details of the formulation are not given here. An interested reader may refer to Abbott (1986) for more information. It is also observed (refer to Fig. 18) that for the stability of the model the following CFL condition must be satisfied:

$$\Delta x/\Delta t > C_w. \tag{2.51}$$

3. Case study and discussions

3.1. Incident wave and computational environment

The model is tested for waves in deep- and shallow-water depth over a domain with flat bottom. Table 1 shows the incident wave and domain conditions.

Here H_0 is the incident wave height, L_0 is the wavelength of corresponding wave period T_0. Different wave conditions are utilized in the following sections. Two different wave sources are used in the numerical implementation of the model as mentioned in Table 1.

SW_2w represents a shallow-water case where only Two-wave ($2L_0$) can enter the computational domain through the incident boundary, they propagate and finally leave the domain through the RHS radiation boundary. The excitation of the incident boundary occurs over two periods ($=2T_0$).

DW_2w stands for a deep-water case where only a Two-wave ($2L_0$) train are allowed to enter the domain and propagate.

SW_iw symbolizes a shallow-water wave source that supplies the domain an amount of Infinite-wave (∞L_0) until the users terminate the computation.

DW_iw denotes a deep-water wave source that transmits an amount of infinite-wave (∞L_0) train to the domain.

3.2. Wave propagation

The model has been tested for the waves propagating in both shallow and deep water. The method is, when *SW_2w* or *DW_2w* has already entered the domain through the incident boundary then the incident wave source is terminated, i.e. only two-waves ($2L_0$) are allowed to enter and propagate through the domain. The propagation of the wave train is studied. The length of the domain is $4.5L_0$.

The propagation of *SW_2w* with wave period (T_0) over the normalized space (x/L_0) is shown in Fig. 3. Fig. 4 shows the propagation of *DW_2w*. In the figures, the

Table 1
Computational conditions

Case	Bathymetry	Incident wave train	h/L_0 (%)	H_0/L_0 (%)
SW_2w	Shallow water	Two-wave ($2L_0$)	37.5	3.0
SW_iw	Shallow water	Infinite-wave (∞L_0)	37.5	3.0
DW_2w	Deep water	Two-wave ($2L_0$)	75.0	3.0
DW_iw	Deep water	Infinite-wave (∞L_0)	75.0	3.0

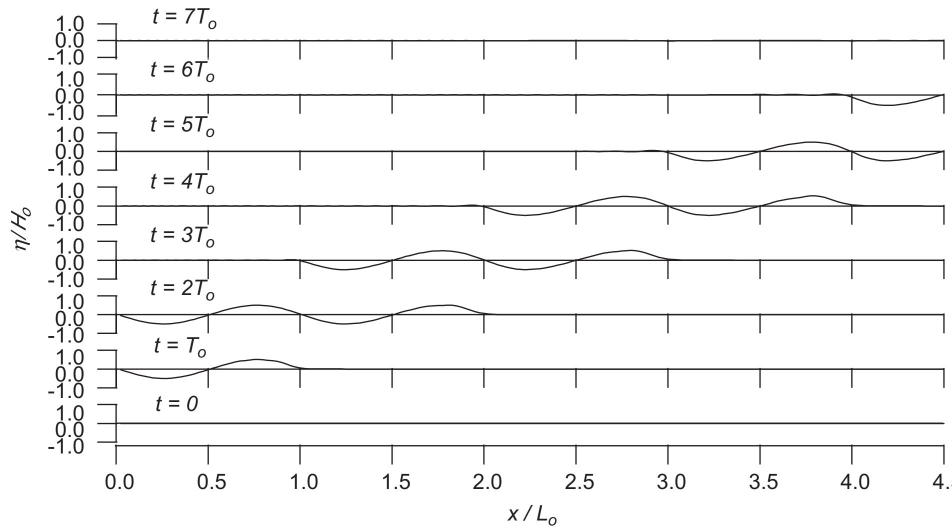

Fig. 3. SW_2w: two-wave train source: instantaneous surface elevations with wave periods over space for shallow-water wave ($T_0 = 0.722$ s, $h = 0.3$ m and $H_0 = 0.024$ m).

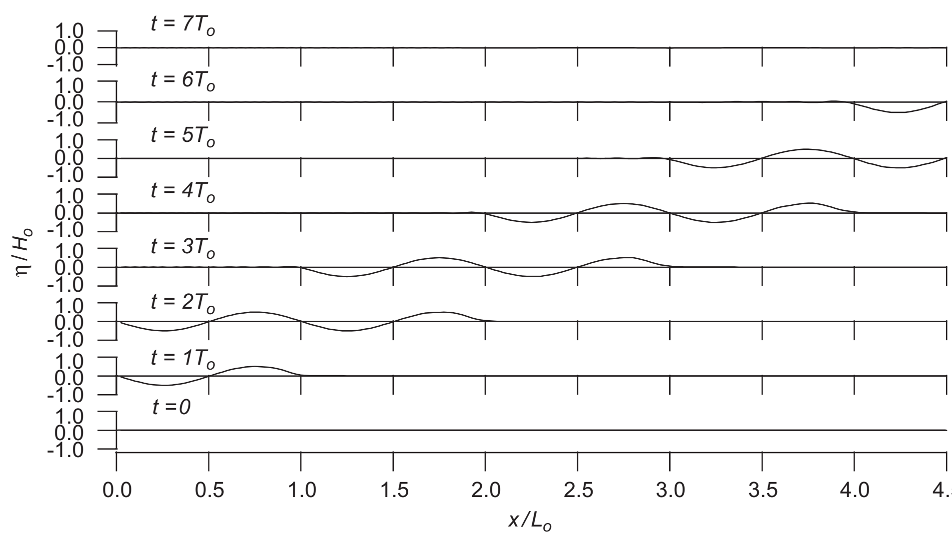

Fig. 4. DW_2w: two-wave train source: instantaneous surface elevations with wave periods over space for deep-water wave ($T_0 = 0.506$ s, $h = 0.3$ m and $H_0 = 0.012$ m).

instantaneous surface elevation η is normalized by the respective incident wave height H_0 and the horizontal distance x is normalized by the incident wavelength L_0. In Figs. 3 and 4 instantaneous surface elevations are plotted for every wave period. It may be observed that with time SW_2w and DW_2w enter the domain, propagate with constant amplitude and finally leave the domain with time in due course.

Figs. 5 and 6, respectively, show the time series of instantaneous surface elevations for SW_2w and DW_2w at specific locations in the domain. Five numerical-wave-gauges (NG) are employed over the domain at equal intervals ($1.125L_0$). NG-1 is at $x = 0.0$ (the incident boundary of the domain), NG-2 is at $x = 1.125L_0$, NG-3 is at $x = 2.25L_0$ (the mid point of the domain), NG-4 is at $x = 3.375L_0$ and NG-5 is at $x = 4.5L_0$ (the transmitted boundary). In the figures the elapsed time t is normalized by the incident wave period T_0. It may be seen in Fig. 5 that SW_2w propagates smoothly over the domain with time. Similar phenomenon is observed for DW_2w case also shown in Fig. 6.

Figs. 7 and 8 show the propagation of SW_iw and DW_iw, that is, when infinite-wave train sources are in use. In this case also wave profiles are plotted for every wave period. These figures show the smooth propagation of the waves in the domain.

Figs. 9 and 10 disclose the time series of the instantaneous surface elevations for SW_iw and DW_iw, respectively, at five different locations from NG-1 to NG-5. Both figures show that with time the waves propagate

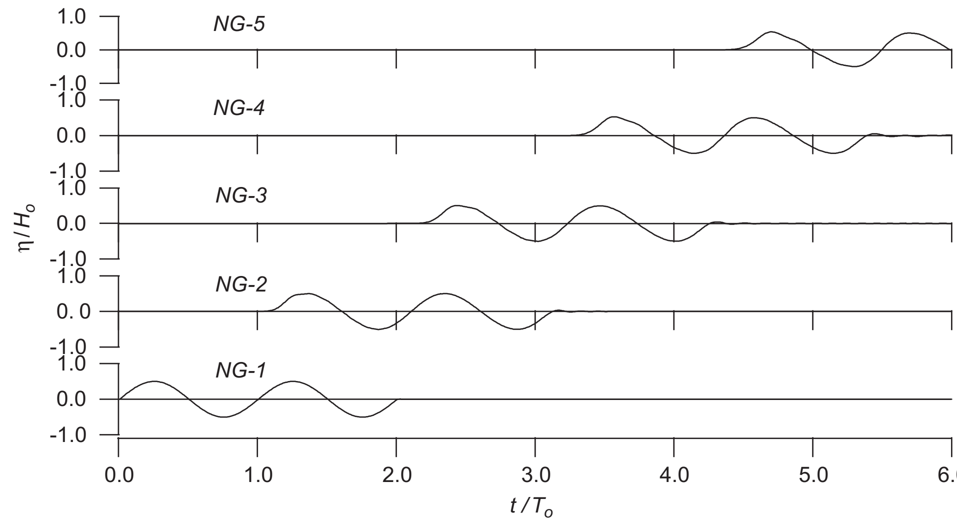

Fig. 5. SW_2w: two-wave train source: time series of instantaneous surface elevations at NG-1 to NG-5 for shallow-water wave ($T_0 = 0.722\,\mathrm{s}$, $h = 0.3\,\mathrm{m}$ and $H_0 = 0.024\,\mathrm{m}$).

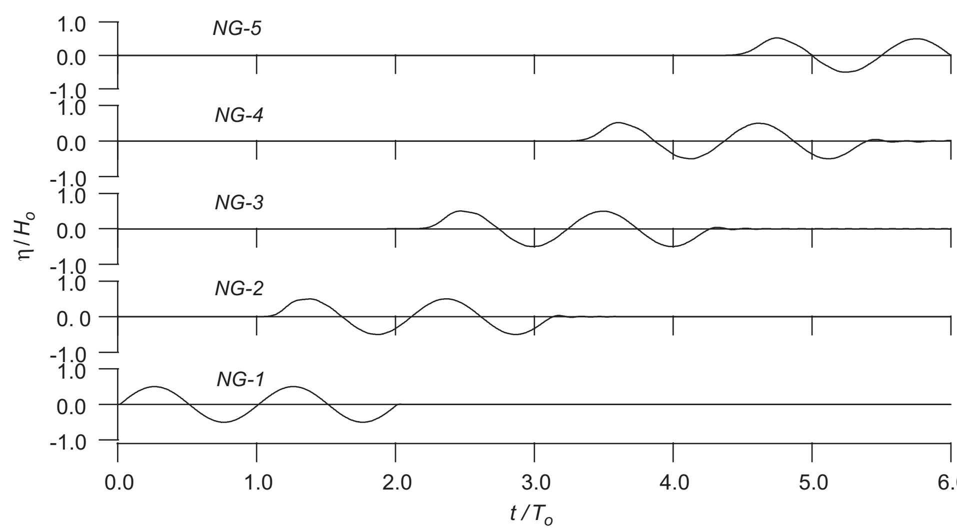

Fig. 6. DW_2w: two-wave train source: time series of instantaneous surface elevations at NG-1 to NG-5 for deep-water wave ($T_0 = 0.506\,\mathrm{s}$, $h = 0.3\,\mathrm{m}$ and $H_0 = 0.012\,\mathrm{m}$).

throughout the domain with the same amplitude as the incident boundary.

3.3. Velocity distribution

Figs. 11 and 12 show the vertical velocity distribution for waves of SW_iw and DW_iw under their crest and trough. The described model is obtained by vertical integration of the governing equations. So we can only obtain a vertically uniform velocity profile from this model. To compute the velocity profiles shown in Figs. 11 and 12 we have assumed a distribution formula that contains the velocity at the free surface multiplied by the pressure response factor as mentioned earlier. In the figures the particle velocities are normalized by the respective incident wave celerity C_0 and the vertical distance z is normalized by the respective water depth h. It may be observed that for the shallow-water case the wave particle velocity is finite up to the bottom but for the deep-water case the particle velocity becomes negligible before it reaches to the bottom. The negative sign in z/h indicates the quantity in the downward direction from the SWL.

3.4. Average energy computation for finite depth case

The potential energy due to the presence of a monochromatic progressive wave train can be computed for a section Δx by subtracting the potential energy in the absence of wave train from the potential energy in the presence of wave train (see for example, Rahman, 1995) as follows (see Fig. 13):

$$\Delta \mathrm{PE} = d\rho g \Delta x \frac{d}{2} - h\rho g \Delta x \frac{h}{2}. \quad (3.1)$$

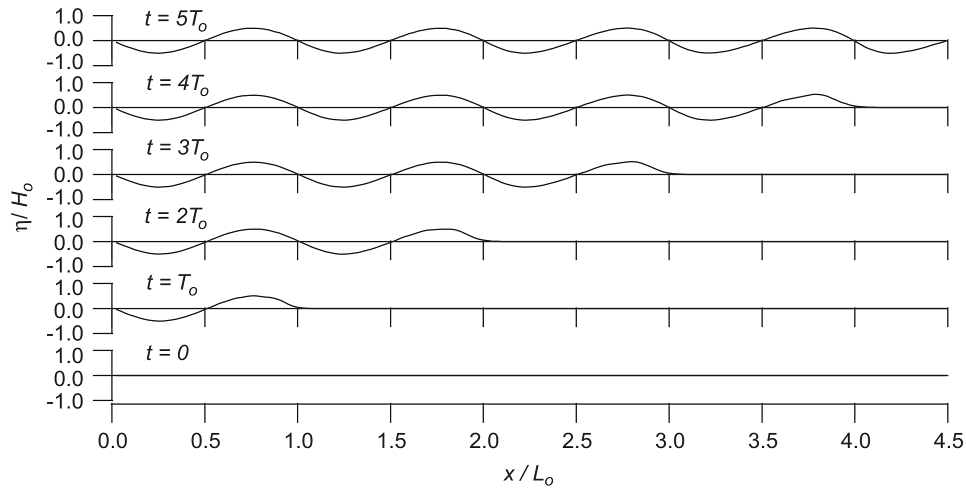

Fig. 7. *SW_iw*: infinite-wave train source: instantaneous surface elevation in space and time for shallow-water wave ($T_0 = 0.722$ s, $h = 0.3$ m and $H_0 = 0.024$ m).

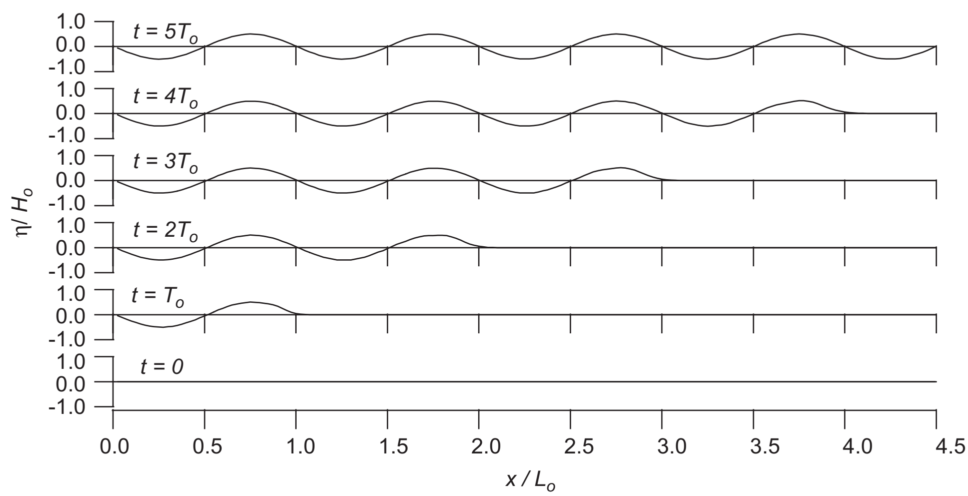

Fig. 8. *DW_iw*: infinite wave train source: instantaneous surface elevation in space and time for deep-water wave ($T_0 = 0.506$ s, $h = 0.3$ m and $H_0 = 0.012$ m).

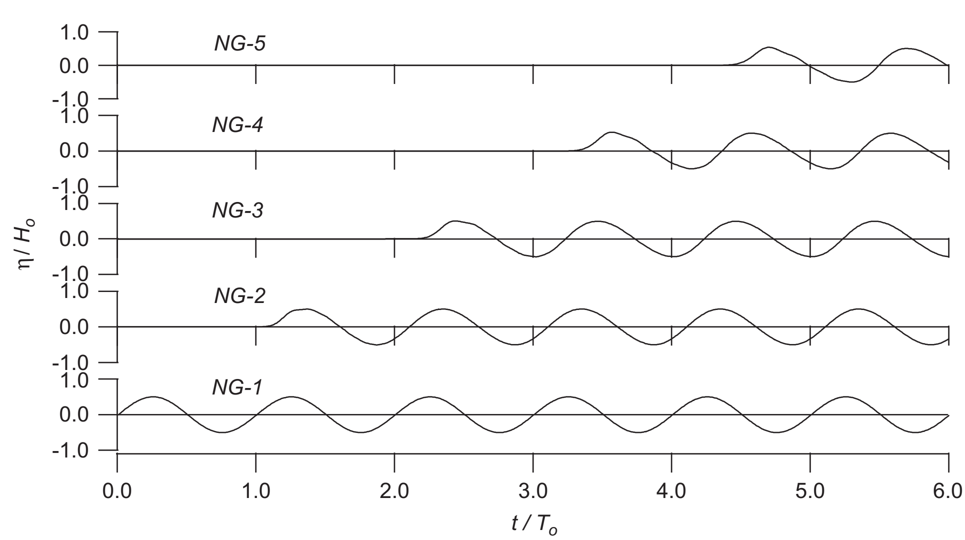

Fig. 9. *SW_iw*: infinite-wave train source: time series of instantaneous surface elevation at NG-1 to NG-5 for shallow-water wave ($T_0 = 0.722$ s, $h = 0.3$ m and $H_0 = 0.024$ m).

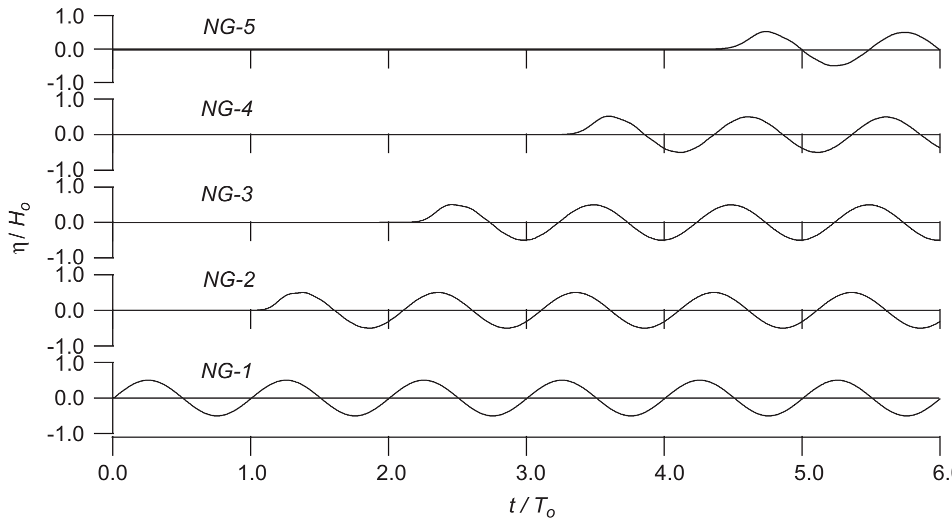

Fig. 10. DW_iw: infinite-wave train source: time series of instantaneous surface elevations at NG-1 to NG-5 for deep-water wave ($T_0 = 0.506\,\mathrm{s}$, $h = 0.3\,\mathrm{m}$ and $H_0 = 0.012\,\mathrm{m}$).

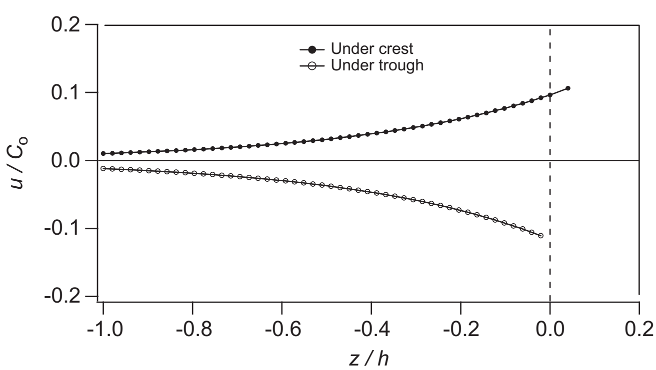

Fig. 11. SW_iw: structure of the vertical velocity distribution under wave crest and wave trough for shallow-water wave ($T_0 = 0.722\,\mathrm{s}$, $h = 0.3\,\mathrm{m}$ and $H_0 = 0.024\,\mathrm{m}$).

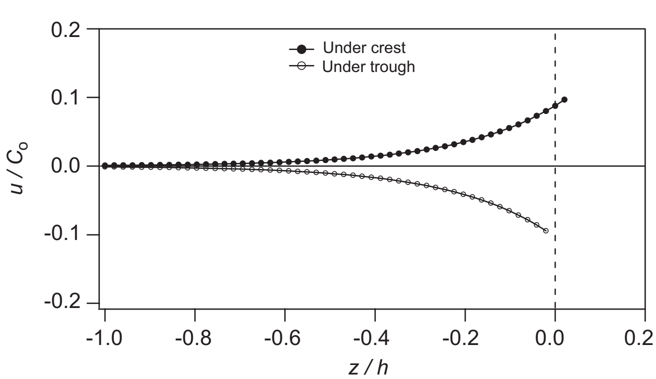

Fig. 12. DW_iw: structure of the vertical velocity distribution under wave crest and wave trough for deep-water wave ($T_0 = 0.506\,\mathrm{s}$, $h = 0.3\,\mathrm{m}$ and $H_0 = 0.012\,\mathrm{m}$).

The average potential energy per unit surface area is then obtained as

$$\mathrm{PE} = \frac{\rho g}{2L_0 T}\int_t^{t+T}\int_x^{x+L_0}(d^2 - h^2)\,\mathrm{d}x\,\mathrm{d}t. \tag{3.2}$$

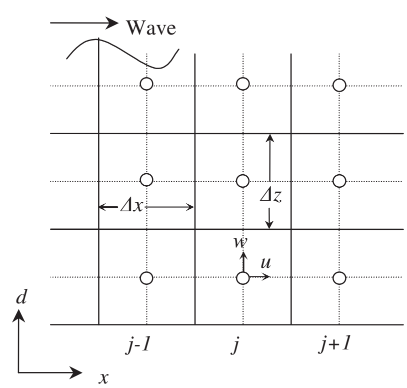

Fig. 13. Numerical mesh for energy computation.

The kinematic energy of a small element of water with length Δx, height Δz and unit width and, having velocity u and w in the horizontal and vertical direction, respectively is

$$\Delta\mathrm{KE} = \frac{\rho}{2}(u^2 + w^2)\Delta x\Delta z. \tag{3.3}$$

Thus the average kinetic energy per unit surface area can be obtained as

$$\mathrm{KE} = \frac{\rho}{2L_0 T}\int_t^{t+T}\int_x^{x+L_0}\int_{-h}^{\eta=0}(u^2 + w^2)\,\mathrm{d}x\,\mathrm{d}z\,\mathrm{d}t. \tag{3.4}$$

To compute the total average energy density (from now on this will be called total energy), we have discretized the domain as shown in Fig. 13. For a spatial grid point the present model computes both kinematic and potential energies at every vertical grid point (shown by O in the figure) over it. Then a summation is made to find out the total energy at that particular spatial location. This method is repeated for all spatial grid points to find the total energy in the whole domain. For a surface wave, the theoretical expression for the total energy per unit area over any water depth has been described by many authors (for example, Lamb, 1945; Sarpkaya and Issscson, 1981; Tucker, 1991). So the average energy density that is produced by a single surface wave can be described by the following *Energy equation*:

$$E = \frac{1}{2}\rho g a^2. \tag{3.5}$$

E_i in the figures is the instant energy computed by the energy equation or by the present model at any time. On the other hand, E_{2w} and E_{iw}, respectively, are the energies computed by the energy equation when two-waves ($2w$) have just entered the domain and maintain their presence in the domain and, when the domain has a infinite number of waves i.e. when the domain has a continuous waves supply.

Figs. 14 and 15 show simple comparisons between the normalized energy distribution over the domain for SW_2w and DW_2w. The solid line shows the energies computed by the present model and the dotted line shows the energies obtained by the energy equation (3.5) for different wave periods. This figure describes that as the wave entering the domain the energy level increases and slowly decreases as the wave train leaves the domain through the transmitted boundary. The highest energy obtained when t/T_0 is in between 2 and 4.5 that is, when both waves are inside the domain. When both waves are just out of the domain the energy level sharply reduces to a value of order 10^{-2} instead of being zero for both SW_2w and DW_2w cases and the energies become zero at or before $t/T_0 = 10$. This may be due to some negligible oscillation that remains in the domain for some time after all the waves disappear. The infinitesimal energies on the right hand sides in Figs. 14 and 15 are the energies due to the presence of these negligible oscillations in the range of $10 \geqslant t/T_0 \geqslant 6.5$. Figs. 14 and 15 indicate that the energies predicted by the model are significantly close to that evaluated by Eq. (3.5) for the respective case. It may be observed that for SW_2w case shown in Fig. 14, when the both waves are in the domain, the model under-predicts the energy to a value of order 10^{-2} and for DW_2w case shown in Fig. 15, the model over-predicts the energies to a value of order 10^{-3}.

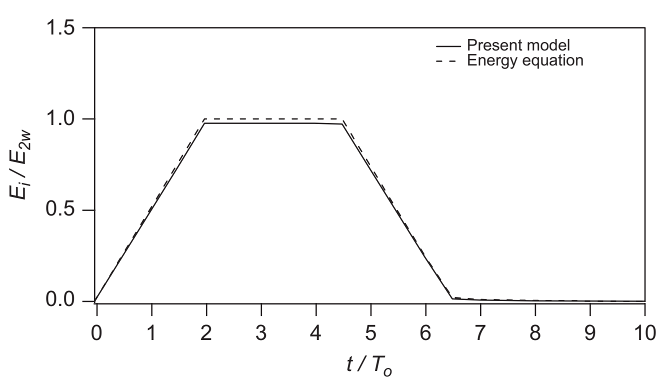

Fig. 14. SW_2w: two-wave train source: comparison of energy between model and computed by the energy equation for shallow-water wave ($T_0 = 0.722$ s, $h = 0.3$ m and $H_0 = 0.024$ m).

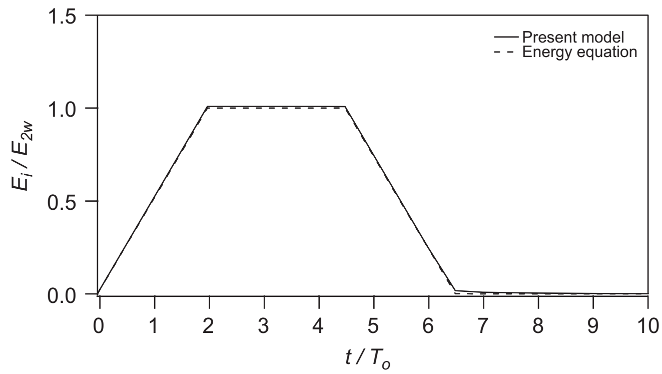

Fig. 15. DW_2w: two-wave train source: comparison of energy between model and computed by the energy equation for deep-water wave ($T_0 = 0.506$ s, $h = 0.3$ m and $H_0 = 0.012$ m).

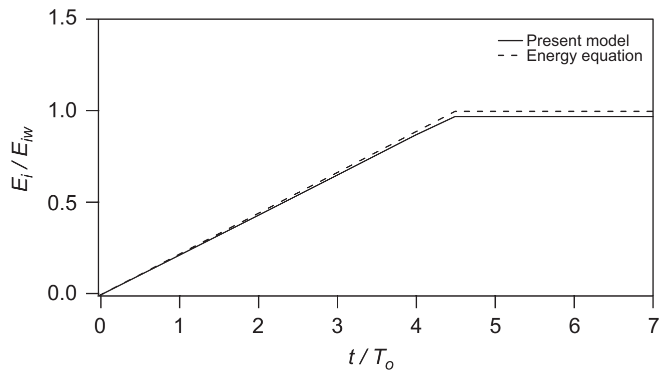

Fig. 16. SW_iw: infinite-wave train source: comparison of energy between model and computed by the energy equation for shallow-water wave ($T_0 = 0.722$ s, $h = 0.3$ m and $H_0 = 0.024$ m).

Figs. 16 and 17 show the normalized energy distribution in the domain for SW_iw and DW_iw. Comparisons of energies between model and that computed by the energy equation (3.5) are shown in these figures. It may be observed that the growth of the energy in the domain is similar as described in Figs. 14 and 15, respectively. Due to the infinite-wave source the energy profile becomes constant when the growth of the energy in the domain is completed, that is, when the domain is fully occupied by the waves. Comparing Figs. 16 and 17 it may be perceived that for the case SW_iw shown in Fig. 16, the model under-shoots the results insignificantly to a value of order 10^{-2} and for case DW_iw shown in Fig. 17, the model returns quasi-identical results (to a value of order 10^{-4}) as computed by Eq. (3.5).

Fig. 18 demonstrates the distribution of the normalized energies for varying $\Delta x/\Delta t$ condition. It may be observed that the model is stable and the results predicted by this model is reliable if Eq. (2.51) remains satisfied.

3.5. Computational error

Proper discretization of the computational domain is one of the important factors in reducing numerical errors. It is

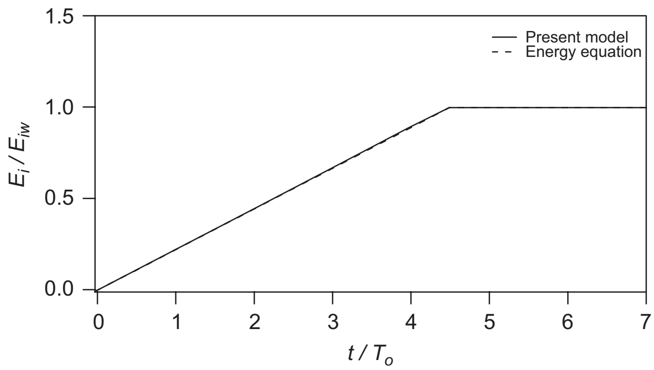

Fig. 17. *DW_iw*: infinite-wave train source: comparison of energy between model and computed by the energy equation for deep-water wave ($T_0 = 0.506$ s, $h = 0.3$ m and $H_0 = 0.012$ m).

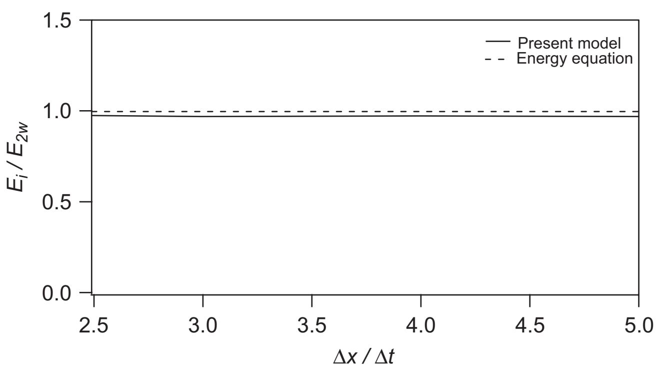

Fig. 18. *SW_iw*: infinite-wave train source: comparison of energies between model and energy equation for varying $\Delta x/\Delta t$ for shallow-water wave ($T_0 = 0.722$ s, $h = 0.3$ m and $H_0 = 0.024$ m).

usual for many traditional numerical model applications that the finer the mesh the better the prediction. A *SW_2w* case is considered here to compute the error level in the surface elevation η. The computational parameters are as before. When the mesh is coarse, that is, the number of computational grid on one wavelength is undersized (less than 40 per wavelength) then some disturbances in the SWL are observed after the wave just left the domain. The is due to unknown numerical errors. The computed errors (mean disturbance amplitude/incident wave amplitude) are found to be in the order of 10^{-6}. On the other hand, when the mesh is fine enough, that is, computational grids are at least 40 in number per wavelength then the numerical error in the surface elevation η over the whole domain is dramatically reduced. Fig. 19 shows that a finer mesh is important to reduce numerical error and to predict better results by this model.

4. Comparisons of the model with Stokes third-order wave theory

A simple comparison is made between the surface elevations obtained from the Stokes third-order wave theory and from the present model for both shallow- and

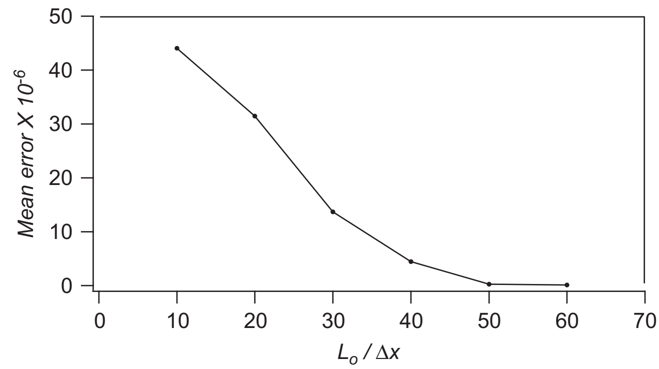

Fig. 19. Mean spatial error (= mean disturbance amplitude/incident wave amplitude) in surface elevation η for shallow-water wave.

Table 2
Computational parameters

Case	Water depth (m)	Wave period (s)	L_0 (m)	h/L_0 (%)	Wave type
*R*1	0.6	1.159	2.0	30	Shallow
*R*2	0.6	0.7158	0.8	75	Deep

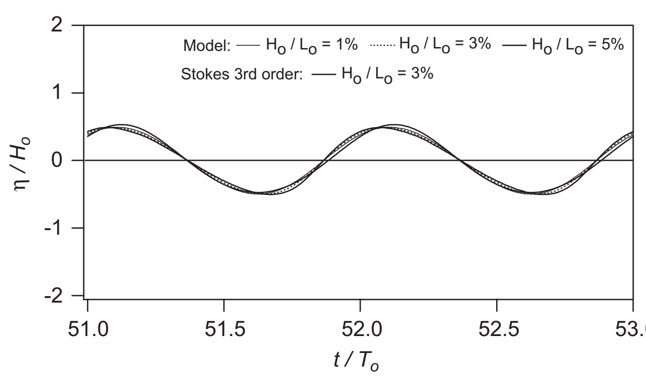

Fig. 20. *R*1: normalised shallow-water ($h/L_0 = 30\%$) surface elevations, model wave steepnesses: $H_0/L_0 = 1\%$, 3% and 5% and Stokes third-order wave steepness: $H_0/L_0 = 3\%$.

deep-water wave cases. The computational parameters are shown in Table 2.

In the comparisons of the shallow-water wave, a wave of period 1.159 s propagates over a water depth of 0.6 m with a relative water depth of $h/L_0 = 30\%$ is utilized and shown by *R*1 in Table 2. Fig. 20 shows a plot of the normalized surface elevations for the wave steepness $H_0/L_0 = 1\%$, 3% and 5% obtained from the present model and normalized surface elevations for Stokes third-order wave theory for $H_0/L_0 = 3\%$. Fig. 21 shows a similar plot where the model wave steepness are $H_0/L_0 = 6\%$, 8% and 10% and Stokes third-order wave steepness is $H_0/L_0 = 8\%$.

On the other hand, for deep-water case shown by *R*2 in Table 2, a wave of period 0.7158 s is assumed to propagate over a water depth of 0.6 m with a relative water depth of $h/L_0 = 75\%$. Fig. 22 shows the model's surface elevation for the steepness $H_0/L_0 = 1\%$, 3% and 5% and Stokes

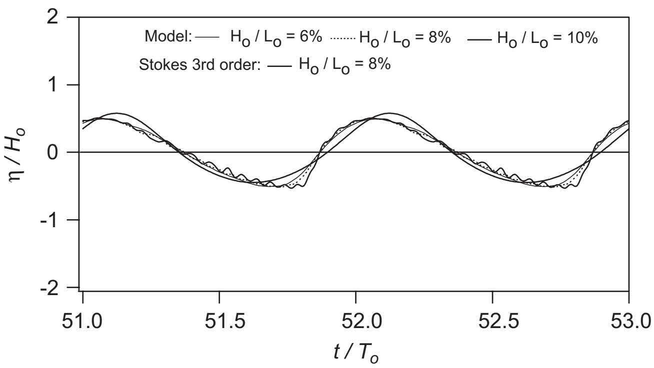

Fig. 21. $R1$: normalised shallow-water ($h/L_0 = 30\%$) surface elevations, model wave steepnesses: $H_0/L_0 = 6\%$, 8% and 10% and Stokes third-order wave steepness: $H_0/L_0 = 8\%$.

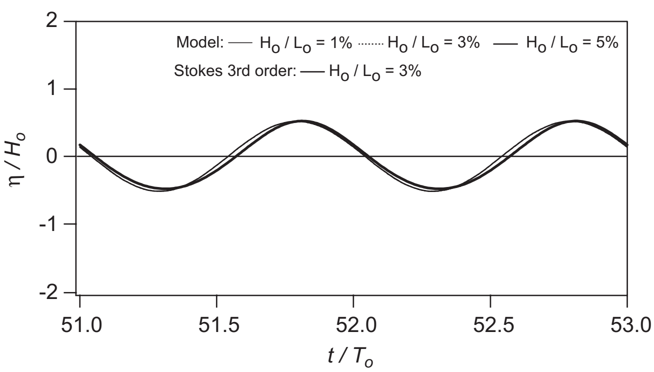

Fig. 22. $R2$: normalised deep-water ($h/L_0 = 75\%$) surface elevations, model wave steepnesses: $H_0/L_0 = 1\%$, 3% and 5% and Stokes third-order wave steepness: $H_0/L_0 = 3\%$.

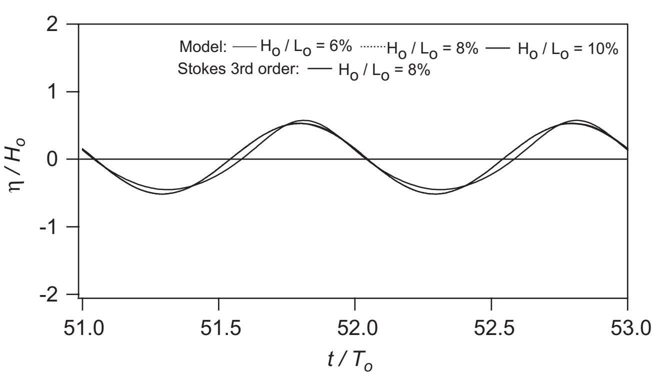

Fig. 23. $R2$: normalised deep-water ($h/L_0 = 75\%$) surface elevations, model wave steepnesses: $H_0/L_0 = 6\%$, 8% and 10% and Stokes third-order wave steepness: $H_0/L_0 = 8\%$.

third-order wave profile with steepness $H_0/L_0 = 3\%$. Fig. 23 shows a plot of surface elevations for steepness $H_0/L_0 = 6\%$, 8% and 10% and Stokes third-order wave steepness $H_0/L_0 = 8\%$. In the figures the surface elevations and the computational times are normalized by the incident wave height H_0 and wave period T_0, respectively.

McCowan (1894) and Hamada (1951) have described that before breaking the maximum shallow-water wave steepness is $14.2\% \tanh(2\pi h/L_0)$. On the other hand, Michell (1893) has reported that the maximum wave steepness that can be achieved by a deep-water wave would be approximately 14.2%. In the computation it is observed that for the shallow-water wave case, see Figs. 20 and 21, the present model gets slowly unstable when the wave steepness is larger than 9%. On the other hand, for the deep-water wave case, results from the model beyond the limiting value for maximum steepness are meaningless.

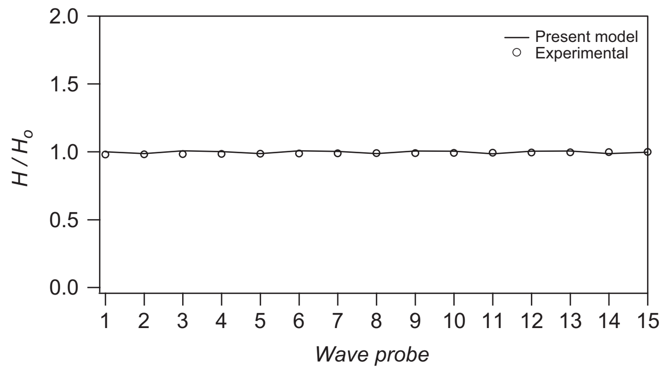

Fig. 24. S1: comparison of the model wave heights with experiment ($T_0 = 1.159$ s, $h = 0.6$ m, $H_0 = 0.06$ m, $h/L_0 = 0.3$, and $H_0/L_0 = 0.03$).

Table 3
Computational conditions and parameters

Case	Water depth (m)	Wave period (s)	H_0 (m)	h/L_0 (%)	H_0/L_0 (%)
$S1$	0.6	1.159	0.06	30	3.0
$S2$	1.0	1.460	0.10	30	3.0

5. Comparisons of the model with experimental results

In order to perceive the validity of the present numerical model we compare the model results with the relevant experimental results in the shallow-water region. Figs. 24 and 25 show these comparisons for two different wave conditions shown in Table 3. In the experiment see Zaman and Togashi (1996), measurements are made at 15 different locations in the wave channel simultaneously. Fig. 24 shows the results for case S1 and Fig. 25 shows the results for case S2. The wave heights at each physical and numerical probe are computed by rms (root-mean-square) method using the respective measured and numerically obtained surface elevation data. The continuous line in Fig. 24 or in Fig. 25 is not an interpolating curve. It joins the computed results from the numerical model.

It is observed in the analyses that the average difference in the wave heights obtained from the model and the experiment is only 0.9% [(Model − Experiment)/Model] for case S1 and 3.6% [(Model − Experiment)/Model] for case S2.

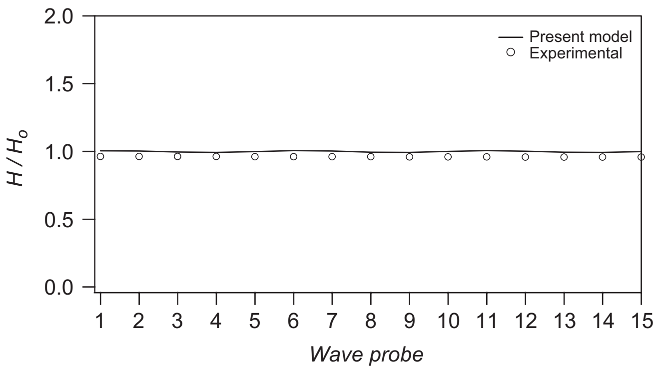

Fig. 25. S2: comparison of the model wave heights with experiment ($T_0 = 1.46$ s, $h = 1.0$ m, $H_0 = 0.1$ m, $h/L_0 = 0.3$, and $H_0/L_0 = 0.03$).

6. Conclusions

A nonlinear numerical model is developed to study the propagation of monochromatic surface wave. The model is developed by the vertical integration of the continuity equation and the equations of motion up to the free surface with proper boundary conditions. The adopted pressure equation and the dispersion relation use the instantaneous water depth instead of still water depth that allows the system to account for the effect of the real time water depth on the solution. The model is applied to study the waves in both shallow- and deep-water regions. Some relevant comparisons are shown between the surface elevations obtained from the model and those obtained from the Stokes third-order wave theory for both shallow- and deep-water wave cases. As an application, the obtained model is tested to study the propagation of the waves, related energy proliferation, vertical velocity distribution and related error prediction. It is found that the prediction of the results by the proposed model is applicable both for shallow- and deep-water wave specially for the cases considered here. The model wave heights for shallow-water wave are compared with the relevant experimental data. The CPU time is exceptionally small in implementing this model on a usual PC.

References

Abbott, M.B., 1986. Computational Hydraulics: Elements of the Theory of Free Surface Flows. Addison-Wesley Longman Publishing Co, Reading, MA, pp. 1–323.

Agnon, Y., Sheremet, A., 1997. Stochastic non-linear shoaling of directional spectra. Journal of Fluid Mechanics 345, 79–99.

Battjes, J.A., 1994. Shallow water wave modelling. International Symposium: Waves—Physical and Numerical Modelling, pp. 1–23.

Beecham, S., Khiadani, M.H., Kandasamy, J., 2005. Friction factors for spatially varied flow with increasing discharge. Journal of Hydraulic Research ASCE, 1–8.

Beji, S., Nadaoka, K., 2004. Fully dispersive nonlinear water wave model in curvilinear coordinates. Journal of Computational Physics 198, 645–658.

Cruz, E.C., Isobe, M., 1994. Numerical wave absorbers for short and long wave modelling. In: Proceedings of the International Symposium on Waves—Physics and Numerical Modelling, vol. 2. University of British Columbia, pp. 992–1001.

Dean, R.G., Dalrymple, R.A., 1992. Water Wave Mechanics for Engineers and Scientists. JBW Printers and Binders, pp. 1–353.

Dronkers, J.J., 1969. Tidal computations for rivers, coastal areas and seas. Journal of Hydraulic Division, Proceedings of ASCE 95 (1), 39–49.

Eldeberky, Y., Madsen, P.A., 1998. Fully dispersive spectral models of triad wave interactions. In: Proceedings of the 26th International Conference on Coastal Engineering (ASCE).

Hager, W.H., 1983. Open channel hydraulics of flows with increasing discharge. Journal of Hydraulic Research 21 (3), 177–193.

Hamada, T., 1951. Breakers and beach erosion. Report of the Transactions of Technical Research Institute, vol. 1, pp. 1–165.

Hedges, T.S., 1976. An empirical modification to linear wave theory. Proceedings of the Institute of Civil Engineers, Part 2 61 (5), 75–579.

Herbers, T.H.C., Burton, M.C., 1997. Non-linear shoaling of directionally spread waves on a beach. Journal of Geophysical Research 102 (C9), 21101–21114.

Horikawa, K., 1988. Nearshore dynamics and coastal processes. University of Tokyo Press, pp. 1–522.

Kaihatu, J.M., Kirby, J.T., 1995. Non-linear transformation of waves in finite water depth. Physics of Fluid 7 (8), 1903–1914.

Lamb, H., 1945. Hydrodynamics, sixth ed. Dover, New York, pp. 1–306.

Madsen, P., Sorensen, O., 1993. Bound waves and triad interactions in shallow water. Ocean Engineering 18, 183–204.

McCowan, J., 1894. On the highest wave of permanent type. Philosophical Magazine Series 5 (38), 351–357.

Michell, J.H., 1893. On the highest waves in water. Philosophical Magazine Series 5 (36), 430–437.

Nwogu, O., 1993. An alternative form of the Boussinesq equations for modelling the propagation of waves from deep to shallow-water. Journal of Waterway, Port, Coastal and Ocean Engineering 1196, 618–638.

Ohyama, T., Kioka, W., Tada, A., 1995. Applicability of numerical models to nonlinear dispersive waves. Coastal Engineering Elsevier Science Publication B. V. 24, 301–311.

Peregrine, D.H., 1967. Long waves on a beach. Journal of Fluid Mechanics 27 (4), 815–827.

Phillips, O.M., 1997. The Dynamics of the Upper Ocean, second ed. University Press, Cambridge.

Rahman, M., 1995. Water Waves. Oxford Science Publications, pp. 1–343.

Sarpkaya, T., Issscson, M., 1981. Mechanics of Wave Forces on Offshore Structures. Van Nostrand Reinhold, New York, pp. 1–651.

Stoker, J.J., 1957. Water Waves. Interscience, New York, pp. 1–567.

Tucker, M.J., 1991. Waves in ocean engineering: measurement, analysis and interpretation. Ellis Horwood Series in Marine Science, pp. 1–431.

Ursell, F., 1953. The long-wave paradox in the theory of gravity waves. Proceedings of the Cambridge Philosophy Society 49, 685–694.

Yu, X., 1990. Study on wave transformation over submerged plate. Ph.D. Thesis, University of Tokyo, 1–153.

Zaman, M.H., Togashi, H., 1996. Experimental study on interaction among waves, currents and bottom topography. Proceedings of the Civil Engineering in the Ocean, JSCE 12, 49–54.

Zaman, M.H., Togashi, H., 1997. Modeling horizontally two dimensional wave-current coexistence field over uneven topography. Proceedings of the Seventh International Offshore and Polar Engineering Conference, ISOPE-97, vol. III, Hawaii, USA, pp. 838–845.